Chemical Science

EDGE ARTICLE

View Article Online
View Journal | View Issue

Cite this: *Chem. Sci.*, 2023, **14**, 14131

All publication charges for this article have been paid for by the Royal Society of Chemistry

A universal orthogonal imaging platform for living-cell RNA detection using fluorogenic RNA aptamers†

Peng Yin, Mingmin Ge, Shiyi Xie, Li Zhang, Shi Kuang* and Zhou Nie *

Received 20th September 2023
Accepted 21st November 2023

DOI: 10.1039/d3sc04957d

rsc.li/chemical-science

MicroRNAs (miRNAs) are crucial regulators of gene expression at the post-transcriptional level, offering valuable insights into disease mechanisms and prospects for targeted therapeutic interventions. Herein, we present a class of miRNA-induced light-up RNA sensors (miLS) that are founded on the toehold mediated principle and employ the fluorogenic RNA aptamers Pepper and Squash as imaging modules. By incorporating a sensor switch to disrupt the stabilizing stem of these aptamers, our design offers enhanced flexibility and convertibility for different target miRNAs and aptamers. These sensors detect multiple miRNA targets (miR-21 and miR-122) with detection limits of 0.48 and 0.2 nM, respectively, while achieving a robust signal-to-noise ratio of up to 44 times. Capitalizing on the distinct fluorescence imaging channels afforded by Pepper-HBC620 (red) and Squash-DFHBI-1T (green), we establish an orthogonal miRNA activation imaging platform, enabling the simultaneous visualization of different intracellular miRNAs in living cells. Our dual-color orthogonal miLS imaging platform provides a powerful tool for sequence-specific miRNA imaging in different cells, opening up new avenues for studying the intricate functions of RNA in living cells.

Introduction

MicroRNAs (miRNAs) are small non-coding RNA molecules that engage in complementary base pairing with non-coding regions in mRNA of various eukaryotes. They are pivotal in post-transcriptional regulation of gene expression, affecting over 60% of protein genes and impacting various physiological processes.[1–8] Dysregulation of miRNAs has been implicated in multiple diseases, including but not limited to lung, cervical, and breast cancers.[6,9,10] Owing to their compact size (19–24 nucleotides) and comparatively more straightforward biological processes than proteins and DNA,[11,12] miRNAs are considered valuable biomarkers for disease diagnosis and therapy targets.[13–17] However, traditional miRNA analysis methods, such as those involving fluorescent hybridization probes (including electrochemical[18–20] and quantitative real-time polymerase chain reaction (qPCR)[21] approaches) and MS2 RNA binding protein-fluorescent protein systems,[22–27] have limitations in terms of probe degradation, delivery challenges, complex kinetics,[21–24] and inability to visualize multiple miRNA targets in a single cell, hindering their effectiveness.[28] Besides, the presence of homologous sequences and the low expression levels of miRNAs in living cells pose challenges to their detection.[29] Additionally, the visualization of multiple miRNA targets in different living cells remained challenging, necessitating the development of more efficient and orthogonal RNA imaging approaches.

Recently, fluorogenic RNA aptamers, also known as fluorescent light-up aptamers, have emerged as a promising alternative for RNA imaging.[30,31] Fluorogenic RNA aptamers are discovered using the systematic evolution of ligands by exponential enrichment (SELEX)[32,33] that fold into specific shapes and specifically activate the fluorescence of non-fluorescent small molecule dyes.[30–33] This property renders fluorogenic RNA aptamers a powerful tool for RNA visualization. Over the past decade, various fluorogenic RNAs, including Spinach,[34] Broccoli,[35] Corn,[36] Mango,[37,38] SRB-2,[39–42] Pepper,[43] Beetroot,[44] RhoBAST[45–47] and Squash,[48] have been developed as genetically encoded RNA sensors, enabling the imaging of metabolites,[49–53] metals,[54] proteins,[55,56] and RNAs in living cells.[57–65] Importantly, a genetically encoded fluorogenic RNA sensor for intracellular RNA imaging comes with minimal interference with the normal cellular processes and exhibits a lower background without a target, contributing to its broad and promising applications.

Successful light-up RNA sensors should exhibit a substantial disparity in fluorescence emission before and after binding to the target RNA. To this end, the current light-up RNA sensors often employ split[60,66,67] or allosteric[59,61,62] design principles to break the RNA aptamer's correct folding conformation, yielding

---

State Key Laboratory of Chemo/Biosensing and Chemometrics, College of Chemistry and Chemical Engineering, Hunan Provincial Key Laboratory of Biomacromolecular Chemical Biology, Hunan University, Changsha 410082, China. E-mail: kuangshi@hnu.edu.cn; niezhou.hnu@gmail.com

† Electronic supplementary information (ESI) available. See DOI: https://doi.org/10.1039/d3sc04957d

low background fluorescence. Huang *et al.* and Ying *et al.* demonstrated RNA aptamer allosteric strategies for RNA imaging and quantitative studies of target RNA in living cells.[62,68] Nevertheless, applying these design methods to other RNA aptamers and various targets entails intricate design challenges. In addition, Wang *et al.*[57] developed the iPepper system, a tandem array of inert Pepper with split principles, for imaging diverse endogenous mRNA. Chen *et al.*[69] used a dynamic analysis strategy that introduced a structure-switching aptamer to monitor the spatiotemporal localization of biomolecules in live systems. However, for the complex intracellular environment, these methods have limitations for simultaneous imaging of multiple target RNAs with distinct fluorescence colors in cells. Therefore, there is a need for a simple and versatile RNA sensor platform capable of orthogonal imaging of multiple miRNAs across diverse living cells.

In this study, we present an orthogonal light-up RNA sensor platform designed for the multiplex imaging of miRNAs. The platform utilizes red-emissive Pepper-HBC620 and green-emissive Squash-DFHBI-1T as imaging modules (Scheme 1). We initially validated the sensor design principle using the Pepper RNA aptamer, wherein introducing a complementary miRNA sequence destroys the HBC-binding loop, thereby preventing its interaction with HBC and resulting in diminished fluorescence. However in the presence of the target miRNA, the Pepper-HBC binding core structure recovers, leading to a significant enhancement in fluorescence. We also incorporated multiple sensor units to amplify the detection signal.

Next, building on the versatility of the sensor design principle, we extended this approach to the Squash aptamer[48] to achieve orthogonal dual-color imaging. The orthogonal light-up RNA sensor platform exhibits sub-nanomolar detection sensitivity for miRNAs within cells and demonstrates the ability to differentiate between target miRNAs. Due to the powerful operability of the sensor design principle, we further enhance its usability by designing it to bind different targets. Overall, our results showcase the feasibility of this orthogonal light-up RNA sensor platform for detecting and imaging intracellular miRNAs within living cells. The simplicity, high signal-to-noise ratio, and versatility of the platform make it a valuable tool for investigating RNA functions within living systems.

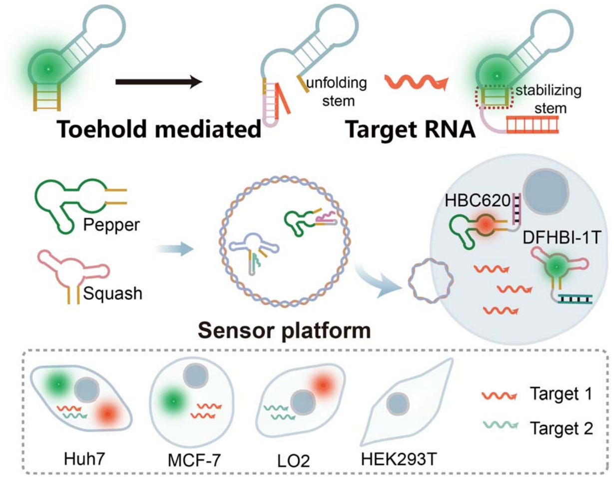

Scheme 1 The orthogonal dual-color fluorogenic RNA aptamer sensor for miRNA imaging in this work.

Results and discussion

Design and optimization of the new Pepper aptamer

The design of the fluorogenic RNA allosteric sensor is typically fraught with intricate optimization processes aimed at acquiring the optimal transducer sequence. Unfortunately, these efforts are often accompanied by challenges, including a relatively low signal-to-noise ratio and insufficient universality. Therefore, to achieve a highly versatile fluorogenic RNA sensor that could readily accommodate various aptamers and adopt a more straightforward design strategy, we initially attempted to design the fluorogenic RNA sensor by screening from a library source. Previous studies have shown that most aptamer SELEX libraries retain an anchor sequence to enhance screening affinity[70] (Fig. S1†). The anchor sequence in the initial random library comprises a 4-base pair stem and a stable UUCG tetraloop. Moreover, this sequence exhibits minimal ligand binding involvement while vital for aptamer folding. Therefore, we propose utilizing this anchor sequence as the switch of the fluorogenic RNA sensor design.

To design the miRNA activation sensor platform, we selected the Pepper RNA aptamer, an uncomplicated and compact RNA molecule. The Pepper aptamer activated the bright fluorescence of HBC[43] (Fig. 1a). The Pepper aptamer was predicted to form a helix, one asymmetric internal loop structure (AILP), an internal loop structure (ILP), and one hairpin loop region (HP)[43] using RNA Structure software (Fig. 1c). Additionally, crystallographic structure determination of the Pepper-HBC revealed that the HBC fluorophore is sandwiched between one non-G-quadruplex quadruple and a noncanonical G·U wobble helical base pair in the ILP structural pocket. Therefore, the ILP structure plays a crucial role in the fluorescent lighting of Pepper-HBC.[71] By comparing with the Pepper SELEX library sequence, it was found that HP as a structural role existed in every library member[43] (Fig. S1†).

Meanwhile, the HP structure of Pepper has much stronger base interactions relative to other structures from the thermodynamic prediction of the NUPACK software (Fig. S2†).

Thus, we hypothesized that the presence of this HP is essential for facilitating the proper folding of Pepper and holds promise as a trigger in miRNA sensor design[72] (Fig. S3 and Table S1†). To explore this potential, we demonstrated two circular permutations to alter the orientation of the 5′ and 3′ ends of the Pepper aptamer. One modification resulted in the direct closure of AILP, thereby opening up the HP structure to form Cp Pepper (Fig. 1b and S1†). However, as determined by fluorescence and the PAGE gel analysis, the Cp Pepper aptamer disrupted effective AILP formation and lacked HBC-binding RNA functionality compared to the original aptamer. Meanwhile, we designed a modified Pepper sequence with a paired stem and stable GAAA tetraloop to padlock the open AILP and create a new Pepper aptamer (Fig. 1b and S1†). The P1 of new Pepper has

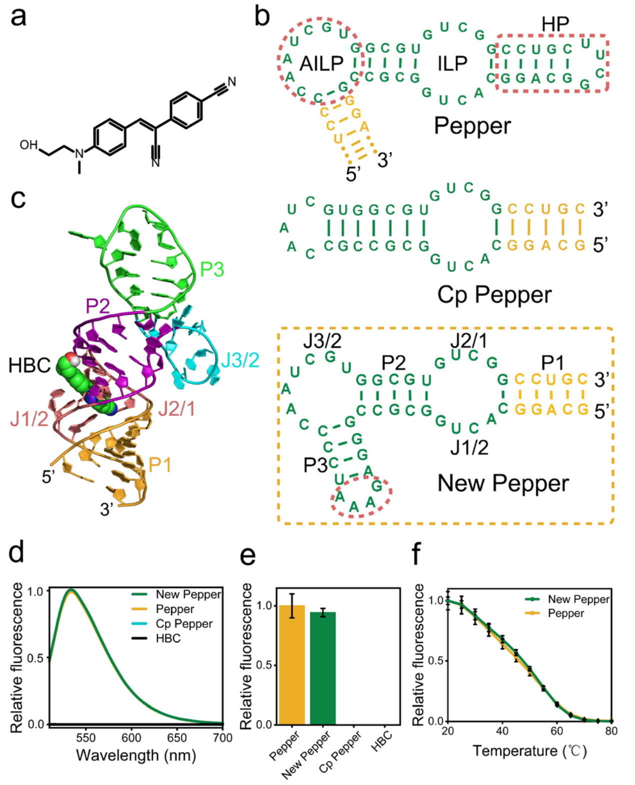

Fig. 1 Design of the new Pepper aptamer. (a) chemical structure of HBC. (b) Predicted secondary structure of Pepper, Cp Pepper and new Pepper for the fluorogenic RNA sensor. (c) The tertiary structure of the new Pepper aptamer. (d) The fluorescence spectra, (e) the relative fluorescence intensity and (f) temperature-dependence of Pepper and the new Pepper aptamer with 5 μM HBC530.

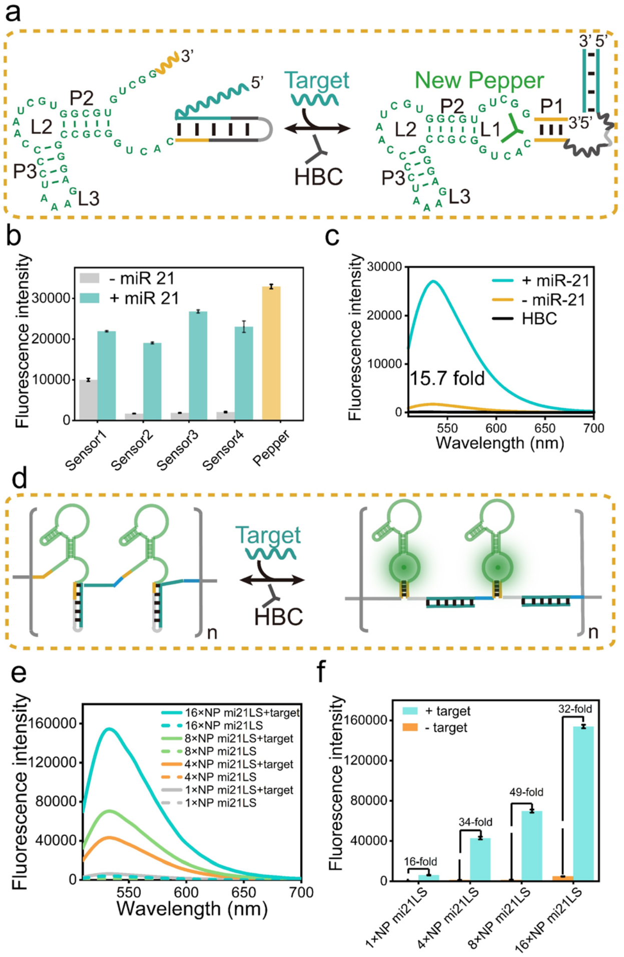

Fig. 2 (a) Schematic illustration of the working principle of miLS. Green bases denote the new Pepper, the yellow lines represent the P1 of new Pepper, and the cyan lines show the target binding region. (b) Fluorescence intensity for the optimization of miLS based on different sequence designs. Fluorescence was measured with 1 μM RNA and 5 μM HBC530 after incubating with 1 μM miR-21. (c) Fluorescence spectra of HBC530 in the presence of 1 μM NP mi21LS and 1 μM NP mi21LS with miR-21. (d) Schematic illustration of the working principle of NP mi21LS tandem arrays. Blue lines denote the linker between the NP mi21LS tandem. (e) Fluorescence spectra of 1×, 4×, 8× and 16× NP mi21LS with and without target RNA (miR-21). (f) Relative fluorescence intensity of the above different tandem arrays of NP mi21LS with and without target RNA. Error bars are standard deviations in three repetitive assays.

a higher contribution to the correct formation of the secondary structure of new Pepper (Fig. S2†). The fluorescence and the PAGE gel analyses demonstrated that new Pepper retained *in vitro* fluorescence properties and thermal stability compared to the original Pepper (Fig. 1d–f, S4 and S5†). In addition, tertiary structures of the HBC binding to RNA aptamer new Pepper in the calculated stable binding state are exhibited in Fig. 1c.

Design of the miRNA sensor using new Pepper

Following the principles elucidated above, we strategically harnessed the P1 stem-loop of the new Pepper aptamer as a folding-dependent domain, integrating it with the complementary sequence of the target miRNA. Employing a toehold-mediated RNA strand displacement,[73] we devised a novel light-up RNA sensor, as illustrated in Fig. 2a and S6a.† This design hindered the proper folding of the Pepper aptamer, leading to disruption of the core structure (L1) of the new Pepper-HBC binding site. Upon hybridizing with its complementary toehold sequence, the target miRNA would release the masked stem and restore the P1 stem of the aptamer, promoting the reformation of the fluorophore binding pocket. The sensor design was generated by NUPACK web and RNA Structure software to predict its structure and achieve minimum free energy. As a result, the properly folded Pepper enabled fluorescence activation in HBC, achieving sensitive detection of miRNA. We have named this miRNA-induced light-up RNA sensor miLS.

Next, to validate the feasibility of miLS as an *in vitro* sensing module, we selected miR-21 as the target miRNA due to its overexpression in various tumor cells.[74] The sensor was constructed by incorporating a miR-21 responsive sequence into the P1 of new Pepper. After simple optimization of the sensor module, sensor 3 was identified as the optimal RNA sensor, named NP mi21LS (Fig. 2b and S7–S9†). In the absence of miR-21, negligible fluorescence was observed at ~530 nm when HBC530 was incubated with this sensor. This observation suggests that new Pepper did not format the correct secondary structure and disrupted the HBC-binding site. However, in the presence of miR-21 (1 μM), a significant increase in fluorescence intensity at 530 nm, approximately 16-fold, was observed, suggesting the successful restoration of the Pepper aptamer structure (Fig. 2c). Compared to other detection methods, this light-up RNA sensor exhibited a higher signal-to-noise ratio (Table S3†). One commonly employed strategy for enhancing the imaging sensitivity of the fluorescence RNA aptamer is to fabricate arrays akin to MS2 cassettes. To improve the sensitivity of the light-up RNA sensors, we attempted to connect NP mi21LS in a series of tandem arrays containing 4×, 8× and 16× miR-21 sensors using the concepts mentioned above. To minimize steric hindrance among the sensors, we used an adenine-rich sequence as the linker to fold Pepper in the tandem arrays properly (Fig. 2d and S10†). As anticipated, the fluorescence intensity showed a proportional increase with the number of arrays utilized. Notably, the signal-to-noise ratio exhibited a marked improvement ranging from 16 to 49 as the number of arrays increased from 1× to 8×. However, an extension of the assay to 16× resulted in a reduction of the signal-to-noise ratio, which could be attributed to a higher likelihood of misfolding of the longer sequences (Fig. 2e and f).

Ulteriorly, the fluorescence intensity of the miR-21 sensor was found to be a dose-dependent behavior within a concentration range of 1 nM to 100 nM. The estimated detection limit was 0.48 nM, reflecting the remarkable sensitivity of this sensor (Fig. S11a†). Selective experiments of NP mi21LS demonstrated its excellent selectivity in complex biological environments, including RNAs (miR-122, miR-224, and iRFP mRNA), proteins (mCherry), and LO2 cell lysate (Fig. S11b†). Furthermore, the PAGE gel analysis and tube imaging more intuitively demonstrated the sensing effect of miR-21 (Fig. S11c and d†). To assess the responsiveness of NP mi21LS to tumor cells, we introduced MCF-7 cells (human breast cancer cells) with high endogenous miR-21 expression levels and HEK293T cells (human embryonic kidney cells) exhibiting low miR-21 expression levels to 500 nM NP mi21LS transfection. Confocal microscopy imaging revealed distinct red fluorescent spots in the cellular cytoplasm of MCF-7 during incubation with HBC620 (Fig. S12†). Besides, when miR-21 was hybridized with anti-miRNA, MCF-7 cells exhibited lower HBC fluorescence (Fig. S12†), NP mi21LS transfected into the majority of the cells and was located in the cytoplasm mostly (Fig. S13†), and HBC showed negligible cytotoxicity to the cells under experimental conditions (Fig. S14†). Therefore, these results demonstrate the exceptional detection performance of this NP mi21LS for miR-21 both *in vitro* and in living cells.

In addition, agarose gel electrophoresis analysis showed that the array sensor and miR-21 mixture migrated slower than the separate array sensor, indicating that the array miR-21 sensor is bound with the target RNA (Fig. S15†). Most importantly, the 16× NP mi21LS showed high fluorescence intensity and sensitivity, which is highly encouraging for subsequent detection of miR-21 in living cells (Fig. S16†). Increasing the number of array sensor repeats resulted in a similar melting temperature (T_m), indicating that thermostability and folding stabilities were maintained even in more extended arrays (Fig. S15†). Collectively, these results proved that the construction of a miLS tandem array can serve as a valuable tool for miRNA imaging.

Engineering of the light-up sensor platform for multiplex miRNA imaging

The correct folding of the fluorogenic RNA aptamer is a crucial step, which depends on the formation of a stabilizing structure framework encompassing elements such as a hairpin structure or stem. Drawing inspiration from these concepts, we applied our miLS design principle to develop a multiplex miRNA sensor and different aptamer imaging platforms (Fig. S17†). By optimizing the sensing module, in this case, by substituting the miR-21 responsive sequence with a miR-122 responsive sequence within the P1 region of new Pepper (Fig. 3a and S6b†), sensor 2 was identified as the optimal RNA sensor, named NP mi122LS, achieving a relatively sensitive light-up sensor that responds to miR-122 (Fig. S18†). In contrast, this sensor exhibited a significantly higher signal-to-background ratio of approximately 44-fold when incubated with 0.5 μM miR-122 and showed remarkable fluorescence recovery efficiency (Fig. 3c). The detection limit was estimated at 0.2 nM (Fig. 3d and S19a†). This sensor displayed negligible fluorescence intensity when exposed to other intracellular substances containing RNAs or proteins (Fig. S19†). Furthermore, the PAGE gel analysis and tube imaging analysis further directly proved the binding of the light-up sensor with miR-122 (Fig. S11c and d†). Notably, miR-122 is the most abundant miRNA in hepatocytes (∼40 000 copies per hepatocyte).[75,76] Consequently, LO2 cells were selected as positive cells, and we observed some red fluorescent foci in the cytoplasm, distinguishing them from the negative HEK293T cells (Fig. 3e and S20†). Moreover, upon treatment with elevated concentrations of anti-miR-122, these cells exhibited diminished fluorescence (Fig. S20†). These results collectively emphasize the ability of NP mi122LS to facilitate the imaging of various RNAs both *in vitro* and within living cells.

Recently, a fluorescence turn-on aptamer Squash, derived from the adenine riboswitch, showed high-folding efficiency *in vitro* and living cells. Squash activated the GFP-like fluorophores dye DFHBI-1T, resulting in an emission maximum at 500 nm. The crystal structure of fluorophore-bound Squash revealed that DFHBI-1T was sandwiched between a base triple and a noncanonical quadruple, effectively limiting non-radiative transitions and restoring the fluorescence. Besides, the P1 stem did not participate in molecular recognition but instead assisted in aptamer folding. This hypothesis was confirmed through nucleotide mutations and structure predictions of this stem of Squash (Fig. S21†).

Subsequently, we continue to employ the same toehold sequence of NP miLS, as detailed previously. MiR-21 was selected as the target RNA and a miR-21 responsive sensing module was obtained by breaking the P1 stem of Squash (Fig. 3b and S22†). When incubating with 1 μM target RNA, the sensor exhibited ∼30-fold increased fluorescence intensity at 500 nm (Fig. 3f). This result suggested that the blocking stem sequence hybridized with the target RNA and restored the folding of Squash. The selectivity and concentration-dependent

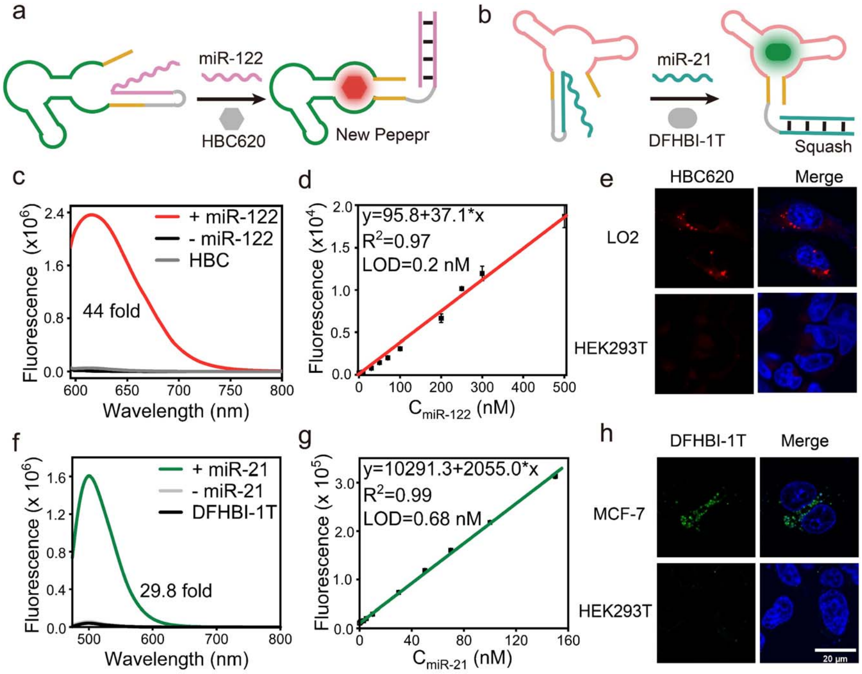

Fig. 3 The mechanism illustration of (a) new Pepper miLS responding to miR-122 and (b) Squash miLS responding to miR-21. (c) Fluorescence spectra of HBC620 in the presence of NP mi122LS and NP mi122LS plus miR-122. (d) The linear relationship between the fluorescence intensity of NP mi122LS and the concentrations of miR-122 ranging from 0 to 500 nM. (e) Confocal imaging results of LO2 and HEK293T cells transfected with the NP mi122LS system when incubated with HBC620. Scale bar, 20 μm. (f) Fluorescence spectra of DFHBI-1T in the presence of Sq mi21LS and Sq mi21LS plus miR-21. (g) The linear relationship between the fluorescence intensity of Sq mi21LS and the concentrations of miR-21 ranging from 0 to 200 nM. (h) Confocal imaging results of MCF-7 and HEK293T cells transfected with the Sq mi21LS system when incubated with DFHBI-1T. Scale bar, 20 μm.

experiment further elucidates the successful construction of Sq mi21LS (Fig. 3g and S23†). Meanwhile, upon incubation of Squash miLS (500 nM) in MCF-7 cells, the imaging results by confocal laser microscopy showed that a majority of green fluorescence spots were observed in living cells (Fig. 3h), and DFHBI-1T showed negligible cytotoxicity (Fig. S14†). Overall, these findings underscore the versatility of the miLS design strategy in enabling the creation of a universal platform for imaging multiple target RNAs and fluorescence aptamers possessing distinct emission wavelengths.

Characterization of orthogonal dual-color fluorogenic sensors

Over the past decade, light-up fluorescence RNA aptamer imaging has provided essential techniques for gaining insight into many RNA functions in living cells. However, the development of light-up RNA aptamer sensors that are characterized by high orthogonality and free from crosstalk is imitated. Furthermore, the characterization of a light-up RNA sensor based on orthogonal aptamers for dual-color imaging of target RNA in mammalian cells is still uncommon, indicating the need for further research in this area (Fig. 4a). Herein, we introduce an orthogonal miLS system using a pair of fluorescence RNA aptamers, Pepper-HBC620, and Squash-DFHBI-1T (Fig. 4b and S24†), thereby enabling dual-color imaging of red Pepper and green Squash.

Next, we explored the feasibility of our miLS platform for orthogonal dual-color imaging of miRNA. By utilizing a system comprising NP mi21LS and Sq mi21LS, along with their respective fluorophores, we observed negligible fluorescence in the range of 450–700 nm in the absence of miR-21. By contrast, this platform incubated with miR-21 at 37 °C exhibited intense fluorescence turn-on at 500 nm or 620 nm, respectively (Fig. 4c). Besides, as shown in Fig. 4d, our system exhibited selectivity in activating the corresponding fluorophore, resulting in distinct fluorescence emission. Additionally, the PAGE gel analysis of the orthogonal miLS system revealed distinct dual-color band shift when subjected to staining with different dyes, stained initially with DFHBI-1T (left), followed by HBC620 (middle), and finally with SYBR green II (right) (Fig. 4e). In addition, the orthogonal miLS facilitated the visualization of green and red fluorescence upon incubation with miR-21 in 96-well plates (Fig. 4f). Upon transfection with this system (500 nM) and incubation with the fluorophores, MCF-7 cells exhibited bright red and green fluorescence (Fig. 4g and h), while HEK293T cells displayed significantly lower fluorescence levels. These results indicate that target RNA can be simultaneously detected using orthogonal miLS in this system. The rational design of this approach represents a significant advancement in RNA bioimaging.

Encouraged by the data mentioned above, we subsequently evaluated the ability of the sensor platform system to discriminate between different miRNAs using a dual-color approach. Specifically, we initially assessed cuvettes containing solutions of 1 μM NP mi122LS-HBC620 pair and Sq mi21LS-DFHBI-1T,

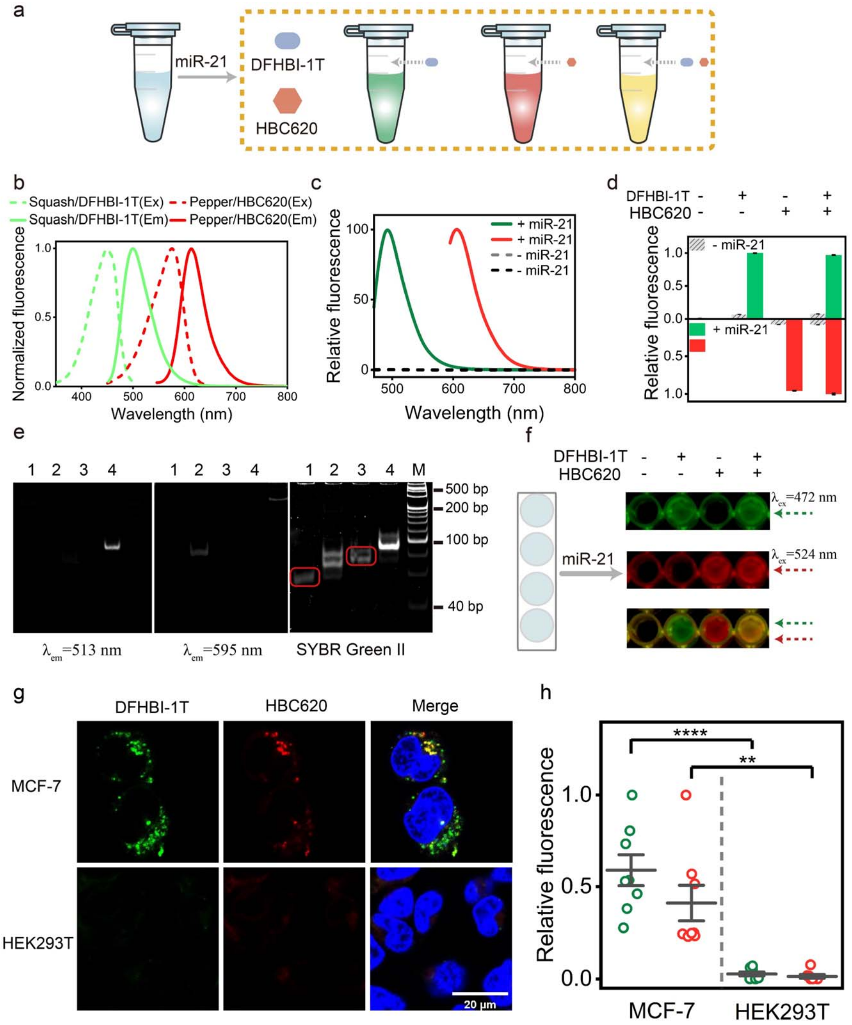

Fig. 4 Characterization of the orthogonal dual-color fluorogenic miLS system. (a) Schematic of the orthogonal dual-color fluorogenic miLS system. (b) Normalized Ex and Em fluorescence spectra of Squash-DFHBI-1T and Pepper-HBC620. (c) Fluorescence spectra of the orthogonal dual-color miLS system with or without miR-21. (d) Relative fluorescence intensity of the orthogonal dual-color miLS system with or without target RNA. Error bars are standard deviations in three repetitive assays. (e) Gel electrophoresis analysis of the orthogonal dual-color miLS system stained using different dyes. Lane 1, NP mi21LS; lane 2, NP mi21LS with miR-21; lane 3, Sq mi21LS; lane 4, Sq mi21LS with miR-21; M denotes molecular weight markers. The bands showing differences in the two gel images are circled in red. (f) Imaging the orthogonal dual-color fluorogenic miLS system with miR-21 in a 96-well plate. (g) Confocal imaging results of the cells transfected with the orthogonal dual-color miLS system when incubated with DFHBI-1T and HBC620. Scale bar, 20 μm. (h) The relative fluorescence of different cells of (g). Values represent means ± SD from 9 independent cells, $^{**}P < 0.01$, $^{****}P < 0.0001$.

each exposed solely to either miR-122 or miR-21 (Fig. 5a). In the presence of miR-21, a slight increase in fluorescence was observed in the green light range. In addition, upon incubation with only miR-122, enhanced fluorescence at 620 nm from HBC620 was detected (Fig. S25†). Real-time kinetics analysis of the fluorescence miLS platform demonstrated gradual increases in green fluorescence from DHFBI-1T upon adding 1 μM miR-21. Meanwhile, incubation with miR-122 prompted a prominent onset of red fluorescence (Fig. 5b).

Next, we analysed the miLS platform using PAGE gel and 96-well imaging to demonstrate its capacity for differential target detection through dual-color orthogonal imaging (Fig. 5c and S25†). Finally, four distinct cell lines (Huh7, MCF-7, LO2, and HEK293T) were selected for testing the miLS platform. Huh7 cells showed overexpression levels of miR-21 and miR-122, while MCF-7 cells displayed high expression of miR-21 and no expression of miR-122. Conversely, LO2 cells exhibited low expression levels of miR-21 and high miR-122, and HEK293T cells served as control cells with no expression of either miR-21 or miR-122. The endogenous expression levels of these two miRNAs in the four cell lines were confirmed *via* qRT-PCR (Fig. S26†). To validate the functionality of the miLS platform system, the above cell lines were transfected with 500 nM of the miLS platform. Confocal laser microscopy images showed a stronger green and red fluorescence signal in Huh7 cells, while MCF-7 cells and LO2 cells detected only green or red fluorescence, each corresponding to their respective miRNA targets, and almost no signal was detected in HEK293T cells

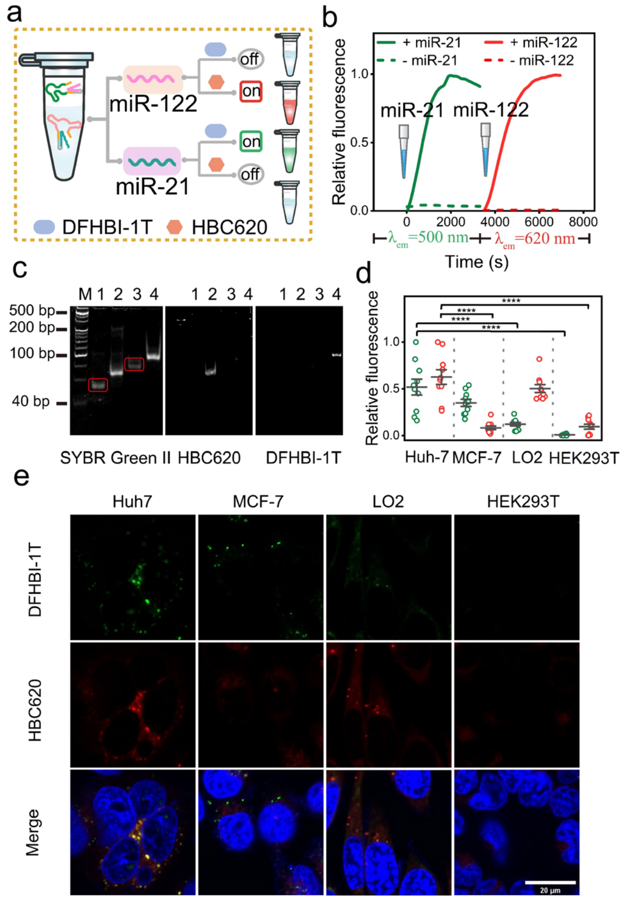

Fig. 5 Characterization of dual-color miLS for miRNA-dependent orthogonal imaging. (a) Schematic of selective imaging of different miRNAs. (b) Fluorescence kinetic analysis of dual-color miLS for miRNA dependent imaging. (c) 10% PAGE analysis of the orthogonal dual-color miLS system with different miRNA-stained dyes. Lane 1, NP mi122LS; lane 2, NP mi122LS with miR-122; lane 3, Sq mi21LS; lane 4, Sq mi21LS with miR-21; M denotes molecular weight markers. The bands showing differences in the two gel images are circled in red. (d) The relative fluorescence of different cells of (e). Values represent means ± SD from 10 fluorescence spots from different cells, $^{****}P < 0.0001$. (e) Confocal imaging results of different cells transfected with the orthogonal dual-color fluorogenic miLS system when incubated with DFHBI-1T and HBC620. Scale bar, 20 μm.

(Fig. 5d and e). These results affirm the successful development of the miLS sensor system capable of activating fluorescence in response to different endogenous target RNA molecules in different cells, which can be visualized using orthogonal dual-color imaging RNA.

Conclusions

In summary, we have developed a novel miRNA-induced light-up RNA sensor (miLS) that enables the visualization of miRNA of interest both *in vitro* and in living cells. The design concept for miLS was inspired by aptamer screening principles, utilizing the screening anchor hairpin structure as the foundational sensor switch. By introducing a miRNA hybrid sequence into the hairpin loop of the aptamer as the toehold domain, we have effectively modulated the sensor response. MiLS exhibits a significant signal-to-noise ratio (>40 fold) *in vitro*, thereby enabling remarkable sensitive and accurate detection of multiple target miRNAs using diverse aptamers with distinct fluorescent colours. The versatility of miLS was further enhanced by its capacity for dual-color orthogonal imaging of miR-21, both *in vitro* and in living cells, by leveraging the integration of Pepper and Squash aptamers with responsive units. Notably, our system exhibits relatively high resolution between the red and green fluorescence channels, thus enabling the dependable differentiation of endogenous miRNA targets in various cellular contexts. By harnessing the potential of this dual-color orthogonal imaging platform, the capability to image different miRNAs as needed, by concurrently employing the corresponding miLS is realized. This flexibility expands the toolbox of light-up imaging techniques and provides a valuable approach for deciphering the intricate physiological processes involving miRNAs in living cells.

Data availability

The data that support the findings of this study are available in the main text and the ESI.†

Author contributions

P. Yin, S. Kuang, and N. Zhou proposed the idea, designed the experiments, and revised the manuscript. P. Yin performed experimental work and wrote the manuscript. M. Ge, S. Xie, and L. Zhang performed most of the assays. All authors contributed to the manuscript.

Conflicts of interest

The author(s) declare that they have no competing interests.

Acknowledgements

This work was supported by the National Key R&D Program of China (2021YFA0910100), the National Natural Science Foundation of China (22034002, 21725503, and 22204047), the Natural Science Foundation of Hunan Province (2023ZK1120 and 2023JJ40122) and the Fundamental Research Funds for the Central Universities. The cell lines used in the study were obtained from the American type culture collection (ATCC).

Notes and references

1 D. P. Bartel, *Cell*, 2009, **136**, 215–233.
2 J. Lu, G. Getz, E. A. Miska, E. Alvarez-Saavedra, J. Lamb, D. Peck, A. Sweet-Cordero, B. L. Ebert, R. H. Mak, A. A. Ferrando, J. R. Downing, T. Jacks, H. R. Horvitz and T. R. Golub, *Nature*, 2005, **435**, 834–883.
3 M. N. Poy, L. Eliasson, J. Krutzfeldt, S. Kuwajima, X. Ma, P. E. MacDonald, S. Pfeffer, T. Tuschl, N. Rajewsky, P. Rorsman and M. Stoffel, *Nature*, 2004, **43**, 226–230.
4 V. Ambros, *Nature*, 2004, **43**, 350–355.

5 L. He and G. J. Hannon, *Nat. Rev. Genet.*, 2004, **5**, 522–531.
6 D. P. Bartel, *Cell*, 2004, **11**, 281–297.
7 T. Jet, G. Gines, Y. Rondelez and V. Taly, *Chem. Soc. Rev.*, 2021, **50**, 4141–4161.
8 Z. He, S. Peng, Q. Wei, S. Jia, S. Guo, K. Chen and X. Zhou, *CCS Chem.*, 2020, **2**, 89–97.
9 B. Mead and S. Tomarev, *Neural Regen. Res.*, 2022, **17**, 516–522.
10 L. Yu, P. Verwilst, I. Shim, Y.-Q. Zhao, Y. Zhou and J. S. Kim, *CCS Chem.*, 2020, **3**, 2725–2739.
11 H. Zhou, Y. Jiang, W. Zhao and S. Zhang, *ACS Appl. Mater. Interfaces*, 2022, **14**, 13070–13078.
12 H. Xu, Y. Zheng, D. Chen, Y. Cheng, X. Fang, C. Zhong, X. Huang, Q. Huang, J. Xu, J. Xu and C. Xue, *Anal. Chem.*, 2022, **95**, 1210–1218.
13 J. Li, S. Tan, R. Kooger, C. Zhang and Y. Zhang, *Chem. Soc. Rev.*, 2014, **4**, 506–517.
14 W. Zhou, D. Li, R. Yuan and Y. Xiang, *Anal. Chem.*, 2019, **91**, 3628–3635.
15 K. Quan, J. Wang, J. Li, K. Wang and J. Huang, *CCS Chem.*, 2021, **4**, 3505–3515.
16 J. Wei, J. Shang, S. He, Y. Ouyang, I. Willner and F. Wang, *CCS Chem.*, 2022, **4**, 3549–3562.
17 Q. Chao, Y. Zhang, Q. Li, L. Jiao, X. Sun, X. Chen, L. Zhu, Q. Yang, C. Shang, R.-M. Kong, G.-C. Fan, Z.-L. Song and X. Luo, *Anal. Chem.*, 2023, **95**, 7723–7734.
18 A. Roychoudhury, J. W. Dear and T. T. Bachmann, *Biosens. Bioelectron.*, 2022, **212**, 114404.
19 X.-L. Zhang, S.-S. Li, Y.-J. Liu, W.-W. Liu, L.-Q. Kong, Y.-Q. Chai, X.-L. Luo and R. Yuan, *Anal. Chem.*, 2023, **95**, 4077–4085.
20 P. Miao and Y. Tang, *CCS Chem.*, 2020, **3**, 2331–2339.
21 C. Chen, D. A. Ridzon, A. J. Broomer, Z. Zhou, D. H. Lee, J. T. Nguyen, M. Barbisin, N. L. Xu, V. R. Mahuvakar, M. R. Andersen, K. Q. Lao, K. J. Livak and K. J. Guegler, *Nucleic Acids Res.*, 2005, **33**, e179.
22 E. Tutucci, M. Vera, J. Biswas, J. Garcia, R. Parker and R. H. Singer, *Nat. Methods*, 2018, **15**, 81–89.
23 M. E. Tanenbaum, L. A. Gilbert, L. S. Qi, J. S. Weissman and R. D. Vale, *Cell*, 2014, **159**, 635–646.
24 E. Bertrand, P. Chartrand, M. Schaefer, S. M. Shenoy, R. H. Singer and R. M. Long, *Mol. Cell*, 1998, **2**, 437–445.
25 H. Y. Park, H. Lim, Y. J. Yoon, A. Follenzi, C. Nwokafor, M. Lopez-Jones, X. Meng and R. H. Singer, *Science*, 2014, **343**, 422–424.
26 T. J. Carrocci and A. A. Hoskins, *Analyst*, 2014, **139**, 44–47.
27 S. Han, B. S. Zhao, S. A. Myers, S. A. Carr, C. He and A. Y. Ting, *Proc. Natl. Acad. Sci. U. S. A.*, 2020, **117**, 22068–22079.
28 S. Tyagi, *Nat. Methods*, 2009, **6**, 331–338.
29 E. Varkonyi-Gasic, R. Wu, M. Wood, E. F. Walton and R. P. Hellens, *Plant Methods*, 2007, **3**, 12.
30 J. R. Babendure, S. R. Adams and R. Y. Tsien, *J. Am. Chem. Soc.*, 2003, **125**, 14716–14717.
31 X. Lu, K. Y. S. Kong and P. Unrau, *J. Chem. Soc. Rev.*, 2023, **52**, 4071–4098.
32 A. D. Ellington and J. W. Szostak, *Nature*, 1990, **346**, 818–822.
33 B. Hall, J. M. Micheletti, P. Satya, K. Ogle, J. Pollard and A. D. Ellington, *Curr. Protoc. Mol. Biol.*, 2009, **88**, 24.2.1–24.2.27.
34 J. S. Paige, K. Y. Wu and S. R. Jaffrey, *Science*, 2011, **333**, 642–646.
35 G. S. Filonov, J. D. Moon, N. Svensen and S. R. Jaffrey, *J. Am. Chem. Soc.*, 2014, **136**, 16299–16308.
36 K. D. Warner, L. Sjekloća, W. Song, G. S. Filonov, S. R. Jaffrey and A. R. Ferré-D'Amaré, *Nat. Chem. Biol.*, 2017, **13**, 1195–1201.
37 E. V. Dolgosheina, S. C. Y. Jeng, S. S. S. Panchapakesan, R. Cojocaru, P. S. K. Chen, P. D. Wilson, N. Hawkins, P. A. Wiggins and P. J. Unrau, *ACS Chem. Biol.*, 2014, **9**, 2412–2420.
38 A. Autour, S. C. Y. Jeng, A. D. Cawte, A. Abdolahzadeh, A. Galli, S. S. S. Panchapakesan, D. Rueda, M. Ryckelynck and P. J. Unrau, *Nat. Commun.*, 2018, **9**, 1–12.
39 L. A. Holeman, S. L. Robinson, J. W. Szostak and C. Wilson, *Fold. Des.*, 1998, **3**, 423–431.
40 M. Sunbul and A. Jäschke, *Nucleic Acids Res.*, 2018, **46**, e110.
41 F. Bouhedda, K. T. Fam, M. Collot, A. Autour, S. Marzi, A. Klymchenko and M. Ryckelynck, *Nat. Chem. Biol.*, 2020, **16**, 69–76.
42 K. T. Fam, R. Pelletier, F. Bouhedda, M. Ryckelynck, M. Collot and A. S. Klymchenko, *Anal. Chem.*, 2022, **94**, 6657–6664.
43 X. Chen, D. Zhang, N. Su, B. Bao, X. Xie, F. Zuo, L. Yang, H. Wang, L. Jiang, Q. Lin, M. Fang, N. Li, X. Hua, Z. Chen, C. Bao, J. Xu, W. Du, L. Zhang, Y. Zhao, L. Zhu, J. Loscalzo and Y. Yang, *Nat. Biotechnol.*, 2019, **37**, 1287–1293.
44 J. Wu, N. Svensen, W. Song, H. Kim, S. Zhang, X. Li and S. R. Jaffrey, *J. Am. Chem. Soc.*, 2022, **144**, 5471–5477.
45 B. Bühler, J. Schokolowski, A. Benderoth, D. Englert, F. Grün, A. Jäschke and M. Sunbul, *Nat. Chem. Biol.*, 2023, **19**, 478–487.
46 M. Sunbul, J. Lackner, A. Martin, D. Englert, B. Hacene, F. Grün, K. Nienhaus, G. U. Nienhaus and A. Jäschke, *Nat. Biotechnol.*, 2021, **39**, 686–690.
47 D. Englert, E.-M. Burger, F. Grün, M. S. Verma, J. Lackner, M. Lampe, B. Bühler, J. Schokolowski, G. U. Nienhaus, A. Jäschke and M. Sunbul, *Nat. Commun.*, 2023, **14**, 3879.
48 S. K. Dey, G. S. Filonov, A. O. Olarerin-George, B. T. Jackson, L. W. S. Finley and S. R. Jaffrey, *Nat. Chem. Biol.*, 2022, **18**, 180–190.
49 H. Kim and S. R. Jaffrey, *Cell Chem. Biol.*, 2019, **26**, 1725–1731.
50 L. Mi, Q. Yu, A. P. K. K. Karunanayake Mudiyanselage, R. Wu, Z. Sun, R. Zheng, K. Ren and M. You, *ACS Sens.*, 2023, **8**, 308–316.
51 G. Zheng, L. Zhao, D. Yuan, J. Li, G. Yang, D. Song, H. Miao, L. Shu, X. Mo, X. Xu, L. Li, X. Song and Y. Zhao, *Biosens. Bioelectron.*, 2022, **198**, 113827.
52 M. You, J. L. Litke and S. R. Jaffrey, *Proc. Natl. Acad. Sci. U. S. A.*, 2015, **112**, E2756–E2765.
53 M. Fang, H. Li, X. Xie, H. Wang, Y. Jiang, T. Li, B. Zhang, X. Jiang, Y. Cao, R. Zhang, D. Zhang, Y. Zhao, L. Zhu, X. Chen and Y. Yang, *Biosens. Bioelectron.*, 2023, **235**, 115411.

54 Q. Yu, J. Shi, A. P. K. K. K. Mudiyanselage, R. Wu, B. Zhao, M. Zhou and M. You, *Chem. Commun.*, 2019, **55**, 707–710.

55 I. Masuda, T. Igarashi, R. Sakaguchi, R. G. Nitharwal, R. Takase, K. Y. Han, B. J. Leslie, C. Liu, H. Gamper, T. Ha, S. Sanyal and Y.-M. Hou, *Nucleic Acids Res.*, 2017, **45**, 4081–4093.

56 Z.-M. Ying, H.-Y. Xiao, H. Tang, R.-Q. Yu and J.-H. Jiang, *Chem. Commun.*, 2018, **54**, 8877–8880.

57 Q. Wang, F. Xiao, H. Su, H. Liu, J. Xu, H. Tang, S. Qin, Z. Fang, Z. Lu, J. Wu, X. Weng and X. Zhou, *Nucleic Acids Res.*, 2022, **50**, e84.

58 D. Li, F. Yang, R. Yuan and Y. Xiang, *Anal. Chim. Acta*, 2020, **1102**, 84–90.

59 S. S. Aw, M. X. Tang, Y. N. Teo and S. M. Cohen, *Nucleic Acids Res.*, 2016, **44**, e92.

60 A. P. K. K. Karunanayake Mudiyanselage, Q. Yu, M. A. Leon-Duque, B. Zhao, R. Wu and M. You, *J. Am. Chem. Soc.*, 2018, **140**, 8739–8745.

61 C.-X. Dou, C. Liu, Z.-M. Ying, W. Dong, F. Wang and J.-H. Jiang, *Anal. Chem.*, 2021, **93**, 2534–2540.

62 Z.-M. Ying, Z. Wu, B. Tu, W. Tan and J.-H. Jiang, *J. Am. Chem. Soc.*, 2017, **139**, 9779–9782.

63 B. Bühler, J. Schokolowski, A. Jäschke and M. Sunbul, *ACS Chem. Biol.*, 2023, **18**, 1838–1845.

64 Y. Peng, L. Shu, X. Deng, X. Huang, X. Mo, F. Du and Z. Tang, *Anal. Chem.*, 2023, **95**, 13762–13768.

65 Y.-P. Zhang, Z.-G. Wang, Y.-F. Tian, L.-H. Jiang, L. Zhao, D.-M. Kong, X. Li, D.-W. Pang and S.-L. Liu, *Angew. Chem., Int. Ed.*, 2023, **62**, e202217230.

66 Z. Wang, Y. Luo, X. Xie, X. Hu, H. Song, Y. Zhao, J. Shi, L. Wang, G. Glinsky, N. Chen, R. Lal and C. Fan, *Angew. Chem., Int. Ed.*, 2018, **57**, 972–976.

67 K. Ren, R. Wu, A. P. K. K. Karunanayake Mudiyanselage, Q. Yu, B. Zhao, Y. Xie, Y. Bagheri, Q. Tian and M. You, *J. Am. Chem. Soc.*, 2020, **142**, 2968–2974.

68 K. Huang, F. Doyle, Z. E. Wurz, S. A. Tenenbaum, R. K. Hammond, J. L. Caplan and B. C. Meyers, *Nucleic Acids Res.*, 2017, **45**, e130.

69 H.-R. Chen, M.-L. Su, Y.-M. Lei, Z.-X. Ye, Z.-P. Chen, P.-Y. Ma, R. Yuan, Y. Zhuo, C.-Y. Yang and W.-B. Liang, *J. Am. Chem. Soc.*, 2023, **145**, 12812–12822.

70 J. H. Davis and J. W. Szostak, *Proc. Natl. Acad. Sci. U. S. A.*, 2002, **9**, 11616–11621.

71 K. Huang, X. Chen, C. Li, Q. Song, H. Li, L. Zhu, Y. Yang and A. Ren, *Nat. Chem. Biol.*, 2021, **1**, 1289–1295.

72 J. S. Paige, T. Nguyen-Duc, W. Song and S. R. Jaffrey, *Science*, 2012, **335**, 1194.

73 Y. Li, X. Teng, K. Zhang, R. Deng and J. Li, *Anal. Chem.*, 2019, **91**, 3989–3996.

74 D. Bautista-Sánchez, C. Arriaga-Canon, A. Pedroza-Torres, I. A. De La Rosa-Velázquez, R. González-Barrios, L. Contreras-Espinosa, R. Montiel-Manríquez, C. Castro-Hernández, V. Fragoso-Ontiveros, R. M. Álvarez-Gómez and L. A. Herrera, *Mol. Ther. Nucleic Acids*, 2020, **20**, 409–420.

75 B. López-Longarela, E. E. Morrison, J. D. Tranter, L. Chahman-Vos, J.-F. Léonard, J.-C. Gautier, S. Laurent, A. Lartigau, E. Boitier, L. Sautier, P. Carmona-Saez, J. Martorell-Marugan, R. J. Mellanby, S. Pernagallo, H. Ilyine, D. M. Rissin, D. C. Duffy, J. W. Dear and J. Díaz-Mochón, *J. Anal. Chem.*, 2020, **92**, 3388–3395.

76 D. De Rie, I. Abugessaisa, T. Alam, E. Arner, P. Arner, H. Ashoor, G. Åström, M. Babina, N. Bertin, A. M. Burroughs, A. J. Carlisle, C. O. Daub, M. Detmar, R. Deviatiiarov, A. Fort, C. Gebhard, D. Goldowitz, S. Guhl, T. J. Ha, J. Harshbarger, A. Hasegawa, K. Hashimoto, M. Herlyn, P. Heutink, K. J. Hitchens, C. C. Hon, E. Huang, Y. Ishizu, C. Kai, T. Kasukawa, P. Klinken, T. Lassmann, C.-H. Lecellier, W. Lee, M. Lizio, V. Makeev, A. Mathelier, Y. A. Medvedeva, N. Mejhert, C. J. Mungall, S. Noma, M. Ohshima, M. Okada-Hatakeyama, H. Persson, P. Rizzu, F. Roudnicky, P. Sætrom, H. Sato, J. Severin, J. W. Shin, R. K. Swoboda, H. Tarui, H. Toyoda, K. Vitting-Seerup, L. Winteringham, Y. Yamaguchi, K. Yasuzawa, M. Yoneda, N. Yumoto, S. Zabierowski, P. G. Zhang, C. A. Wells, K. M. Summers, H. Kawaji, A. Sandelin, M. Rehli, Y. Hayashizaki, P. Carninci, A. R. R. Forrest and M. J. L. de Hoon, *Nat. Biotechnol.*, 2017, **35**, 872–878.